Controlled single-spin transport in thermally driven molecular devices containing graphene electrodes modulated by quantum resonance

Y. S. Liu [1], X. L. Zou,[2] Y. J. Dong,[1,*] H. L. Yu,[1] J. Zhang [1], X. F. Wang,[2] and X. F. Yang[1,†]
[1]*School of Electronic and Information Engineering, Changshu Institute of Technology, Changshu 215500, China*
[2]*School of Physical Science and Technology, Soochow University, Suzhou, Jiangsu 215006, China*

(Received 29 March 2020; revised 27 July 2020; accepted 14 September 2020; published 14 October 2020)

Resonance effects play an important role in the transport properties of low-dimensional systems. Here, we investigate the thermally driven spin-transport properties of ruthenium-terpyridine molecular devices, where the molecule is linked to graphene electrodes by the carbon atomic chains from two sides. The results show that an odd-even oscillating behavior of the transmission spectra and a perfect spin-filtering effect at the Fermi level are observed in the ruthenium-terpyridine molecular devices. Furthermore, the negative differential thermoelectric resistance more easily appears in the long even-numbered carbon atomic chains, and the sign of the thermally driven single-spin current can be tuned via the temperature. Such a behavior is attributed to the competition between the Breit-Wigner and Fano resonances in the vicinity of the Fermi level for the contributions of the thermally driven current. In brief, here we present an alternative to control the thermally driven single-spin current in molecular devices via quantum effect.

DOI: 10.1103/PhysRevB.102.155415

I. INTRODUCTION

Molecular electronics, in which a single or a small assembly of molecules is used for designing functional electronic devices, is one of the promising avenues to reduce the size of electronic devices. In addition, molecular electronics also provides an ideal test bed to examine the transport phenomena at the atomic and molecular scale. Until now, some interesting theoretical and experimental results on transport properties such as rectification [1], negative differential resistance [2], shot noise [3], thermoelectric effects [4–6], and quantum cooling effects [7], have been reported in various molecular devices.

The Fano effect arises from the quantum interference between two competing transport pathways, which can be observed in atoms [8], bulk solids [9], photonic crystal slabs [10], semiconductor quantum dots [11,12], or ultracold atom systems [13]. A typical characteristic of the Fano resonance is the unique asymmetric line shape, and the asymmetry is due to the interaction of a discrete state with a continuum of propagation modes. When a π-conjugated molecule is sandwiched between two metallic electrodes, a weak Fano resonance appears in the transmission spectrum [14]. Since the transmission function has a rapid change near the Fano resonance, the thermoelectric effects can be obviously enhanced [15–17]. It should be noted that some experimental and theoretical works have demonstrated that graphene might serve as the ideal electrode material, and then the performance of molecular devices could be further improved [18–23]. Compared with traditional three-dimensional (3D) metal electrodes, one definite advantage of single-layer two-dimensional (2D) graphene electrodes is that a stable covalent coupling mode can be formed between the molecule and graphene electrodes [19]. When graphene is tailored into the graphene nanoribbon, the inherent edge magnetism can be introduced in molecular devices [24]. The ability to control the spin transport in the molecular devices is very important to molecular spintronics. Saraiva-Souza *et al*. found a spin-resolved destructive interference feature in a polyacetylene chain bridging zigzag graphene nanoribbons (ZGNRs), where a gate voltage was applied to realize the on and off of the transport for the spin-resolved electrons [25]. In our previous study, a giant spin thermoelectric effect was achieved in all-carbon devices composed of a graphene nanoflake sandwiched between two ZGNRs [26]. In 2008, a pioneering experimental work was reported, where the spin Seebeck effect (SSE) was detected in ferromagnetic materials [27]. Since then, a great deal of theoretical and experimental studies on the SSE have been reported in various ferromagnetic systems or low-dimensional quantum devices [28–32]. Recently, a pure spin current was generated in thermally driven dimer-based molecular junctions in the absence of the electric bias, where a negative differential thermoelectric resistance (NDTR) and a perfect spin-filtering effect have been observed in chromocene dimer-based and manganocene dimer-based molecular junctions [33].

In this paper, we present a study of spin-resolved transport properties through ruthenium(Ru)-terpyridine molecular devices, which is a two-probe model constructed by a molecule that linked to ZGNR electrodes by the carbon atomic chains (CACs) from two sides. Tuning the length of the CACs, the spin-resolved transmission function at the Fermi level shows an odd-even oscillating behavior, where a high conductance is observed for the odd-numbered CACs and a low

*yjdong@cslg.edu.cn
†xfyang@cslg.edu.cn

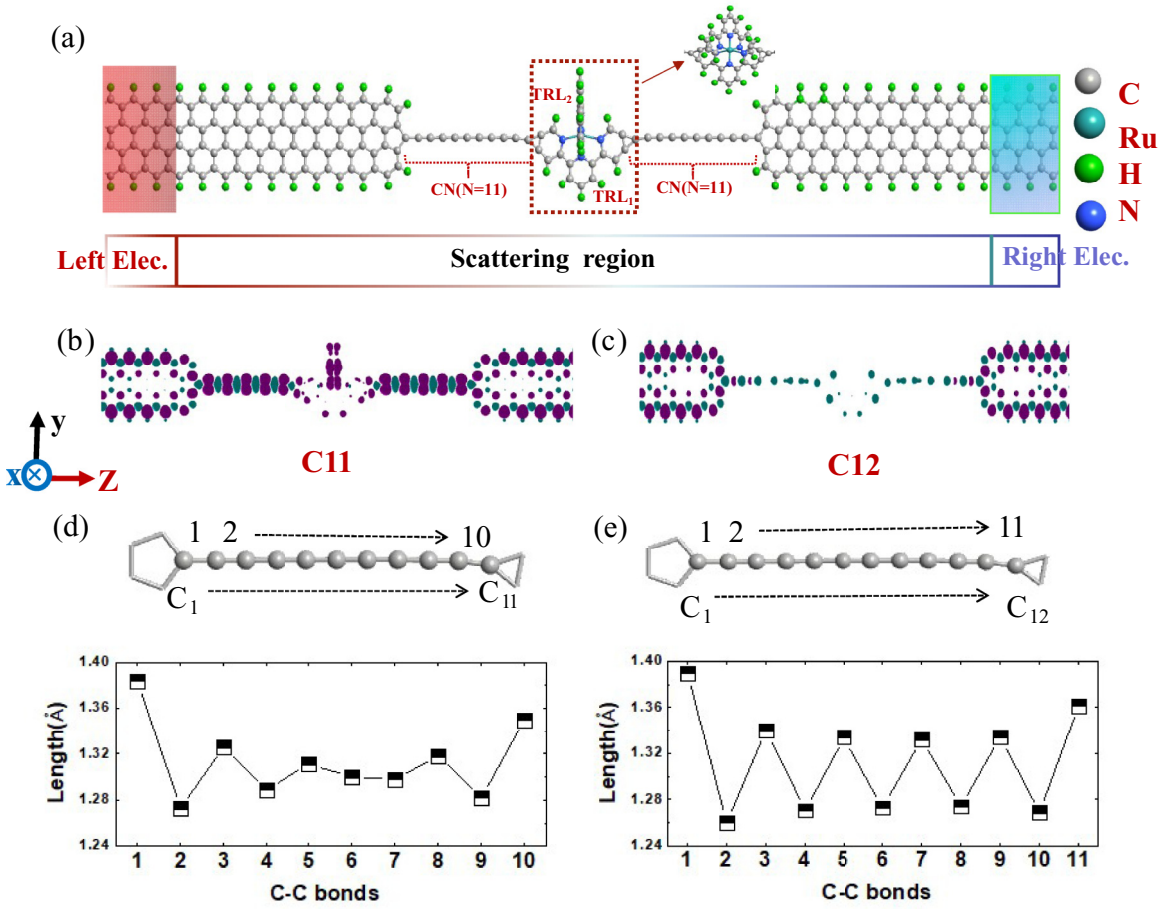

FIG. 1. (a) Schematic representation of the two-probe atomic model of the Ru-terpyridine molecular device, where each carbon atomic chain between the molecule and ZGNR electrodes involves 11 carbon atoms. (b), (c) The isosurface of the spin density, the difference between spin-up and spin-down charge densities for the C11 and C12 Ru-terpyridine molecular device, respectively. A cutoff value of 0.003 eÅ^{-3} is used in the isosurface plot. Dark red and dark green colors stand for the up-spin and down-spin components. (d), (e) The relaxed lengthes of C–C bonds for the C11 and C12 chains, respectively.

conductance for the even-numbered CACs. Moreover, a perfect spin-filtering effect is also observed, where the spin-up channels are opened and the spin-down channels are closed. When a temperature difference is provided, the spin-up electrons or holes are driven from one ZGNR electrode to the other ZGNR electrode through the central molecule. A finding highlight is that the NDTR appears in the molecular junctions with the even-numbered CACs, and here the sign of the thermally driven spin-up current can be changed from a negative value to a positive value for the long even-numbered CACs as the temperature increases. Such a behavior is attributed to the appearance of the Breit-Wigner (BW) resonance below the Fermi level and the Fano resonance above the Fermi level. At the low-temperature regime, the BW resonance has a main contribution to the spin-up current, and as the temperature is further increased, the Fano resonance plays a key role in the spin-up current.

II. MODEL AND CALCULATION METHOD

With the development of preparation technology, the long CACs linked to graphene or graphene nanoribbons can be fabricated in experiments [34,35] and the electrical transport in CACs could be measured by using a scanning tunneling microscopy tip in a transmission electron microscopy stage [36]. As an example, we depict the schematic representation of the Ru-terpyridine molecular device with the odd-numbered CACs in Fig. 1(a). For the sake of simplicity, in the following we will employ the number of the carbon atoms in the CACs to label the Ru-terpyridine molecular device. Therefore, CN represents the Ru-terpyridine molecular device with the N-numbered CACs. It should be noted that the central molecule includes two terpyridine ligands: one terpyridine ligand (labeled TRL_1) is directly linked to the CACs, and the other terpyridine ligand (labeled TRL_2) is coupled to Ru ion which is coordinated to six nitrogen atoms of the two terpyridine ligands. One can clearly see the geometric structure of the Ru-terpyridine molecule when it is rotated by a certain angle along the y axis [see the inset of Fig. 1(a)]. The geometrical optimizations and the spin-resolved electronic transport properties of the Ru-terpyridine molecular device with different lengths of CACs are calculated by a first-principles package (ATOMISTIX TOOLKIT) [37,38], which is based on the density-functional theory and nonequilibrium Green's function methods. Troullier-Martins norm-conserving pseudopotential is employed to expand the

valence state of electrons. We choose the spin generalized gradient approximation to be the exchange-correlation functional, and the wave functions of all atoms are expanded by double-zeta polarized basis set. The k-point sampling is 1, 1, and 100 in the x, y, and z directions, respectively, and the cutoff energy is set to be 150 Ry. Based on the nonequilibrium Green's function methods, we can write the spin-resolved transmission function by [39]

$$\tau_\sigma(\epsilon) = \mathbf{Tr}\left(\Gamma_{\mathrm{L},\sigma} \mathrm{G}^{\mathrm{R}}_\sigma \Gamma_{\mathrm{R},\sigma} \mathrm{G}^{\mathrm{A}}_\sigma\right), \tag{1}$$

which represents the transport probability of electrons or holes with the spin index σ at the energy ϵ from the left electrode to the right electrode via the central molecule. $\Gamma_{\mathrm{L(R)},\sigma}$ in Eq. (1) denotes the level broadening function from the coupling effect of the left (right) electrode to the central scattering region. $\mathrm{G}^{\mathrm{R}}_\sigma$ in Eq. (1) is the retarded Green's function of the scattering region that considers the contributions from the left and right electrodes, and $\mathrm{G}^{\mathrm{A}}_\sigma[=](\mathrm{G}^{\mathrm{R}}_\sigma)^\dagger]$ denotes the advanced Green's function. When a temperature difference is applied across the two-probe device, the thermally driven current with the spin index σ can be calculated by the Landauer-Büttiker equation,

$$I_\sigma = \frac{e}{h}\int_{-\infty}^{+\infty} \tau_\sigma(\epsilon)[f_L(\epsilon,\mu,T_L) - f_R(\epsilon,\mu,T_R)]d\epsilon, \tag{2}$$

where the left and right electrodes have the same electrochemical potential μ and $f_{L(R)}$ denotes the Fermi-Dirac probability function of the left (right) electrode,

$$f_{L(R)}[\epsilon,\mu,T_{L(R)}] = \frac{1}{exp[(\epsilon-\mu)/k_B T_{L(R)}]+1}, \tag{3}$$

where k_B is the Boltzmann constant and $T_{L(R)}$ is the temperature of the left (right) electrode. Once the temperature difference $\Delta T(=T_L - T_R)$ is not zero, $f_L - f_R$ has significant nonzero values near the electrochemical potential μ. As a result, when the nonzero transmission coefficient approaches or enters the energy region, the electrons or holes can be driven from one electrode to the other electrode via the central scattering region.

III. RESULTS AND DISCUSSIONS

It should be noted that ZGNRs have an antiferromagnetic (AFM) ground state with zero net spin, and then their practical applications in spintronics are limited. However, the AFM ground state of the ZGNRs can be converted to the ferromagnetic (FM) state by using an external magnetic field [40]. Therefore, in this paper, the ZGNR with the FM state is chosen to be the electrode. As examples, we plot the spin density ($\Delta\rho = \rho_\uparrow - \rho_\downarrow$) for the C11 and C12 Ru-terpyridine molecular devices in Figs. 1(b) and 1(c), respectively. Here $\rho_{\uparrow(\downarrow)}$ represents the spatial spin-up (spin-down) charge density. The results show that the magnetization of the ZGNR electrodes mainly resides on the edge of the ZGNR, which is in good agreement with the results reported in Ref. [41]. The magnetism of the CACs inserted ZGNR and Ru-terpyridine molecule depends on the parity of the chain. For the odd-numbered CACs, there are even-numbered C–C bonds, and therefore the exact alternation of single and triple bonds cannot be formed. As shown in Fig. 1(d), in this case the C–C bond type for a C11 chain changes from a single/triple type (see two ends of C11 chain) to a double/double type (see the middle of the C11 chain). As a result, some uncompensated charges are delocalized on the odd-numbered CACs and a net magnetic moment is achieved. However, for the even-numbered CACs, an exact alternation of single and triple bonds is formed [see Fig. 1(e)] and all C–C bonds are saturated and no magnetism is expected for the ideal infinite CACs. As a consequence, less spin accumulates in the even-numbered CACs.

The energy-dependent spin-resolved transmission function $\tau_\sigma(\epsilon)$ can be calculated by Eq. (1). In Figs. 2(a)–2(g), we plot $\tau_\sigma(\epsilon)$ as a function of the energy ϵ for the Ru-terpyridine molecular devices containing the CACs with different lengths. From these numerical results, it is found that an obvious characteristic in the transmission spectra is the perfect half-metallic property in the wide energy region in the vicinity of the Fermi level, where the spin-up channels are opened and the spin-down channels are closed. Therefore, a perfect spin-filtering effect is achieved, which mainly originates from the fact that the two CACs are connected to symmetric ZGNR electrodes along the midplane between the two edges [42]. In this case, only those electrons with the symmetric wave functions with respect to the x-z plane can be transported to CACs from the ZGNR electrode. Considering the spin degree of freedom, we can conclude that only spin-up carriers are allowed to transport when the energy range is limited in the vicinity of the Fermi level, while the spin-down carriers are almost completely blocked. In addition, the key finding is that the spin-up transmission spectra near the Fermi level is composed of the BW and Fano resonance peaks. For the even-numbered CACs, one spin-up BW resonance peak appears below the Fermi level and one spin-up Fano resonance peak is located above the Fermi level [see Figs. 2(a), 2(c), 2(e), and 2(g)]. However, for the odd-numbered CACs, there are two spin-up Fano resonance peaks and a BW resonance peak above the Fermi level. In addition, we also plot the spin-up and spin-down transmission functions at the Fermi level as a function of the lengths of the CACs in Fig. 2(h). Indeed, an incredibly small value of the spin-down transmission function is observed, while the spin-up transmission has a relatively large value. In addition, we also find that the spin-up transmission function possesses an odd-even oscillating behavior as the length of the CACs increases. A high spin-up transmission probability is observed for the odd-numbered CACs and a low spin-up transmission probability appears in the even-numbered CACs. Meanwhile, the spin-down transmission function has a similar oscillating behavior as the length of the CAC increases, but keeps an extremely low value. In the bottom panel of Fig. 2, we plot the spin-resolved local density of states (LDOS) at the Fermi level for the C11 and C12 Ru-terpyridine molecular device. Obviously, the spin-down LDOS is completely absent in the scattering region (see LDOS at B and D), resulting in a very low value of the spin-down transmission function. However, the spin-up LDOS spreads over the whole device, meaning that the spin-up carriers can relatively easily transport through the scattering region from one electrode to the other electrode (see LDOS at A and C). Compared with the point C, the more LDOSs appear in the point A. Therefore, the transmission probability atpoint A is larger than that at point C.

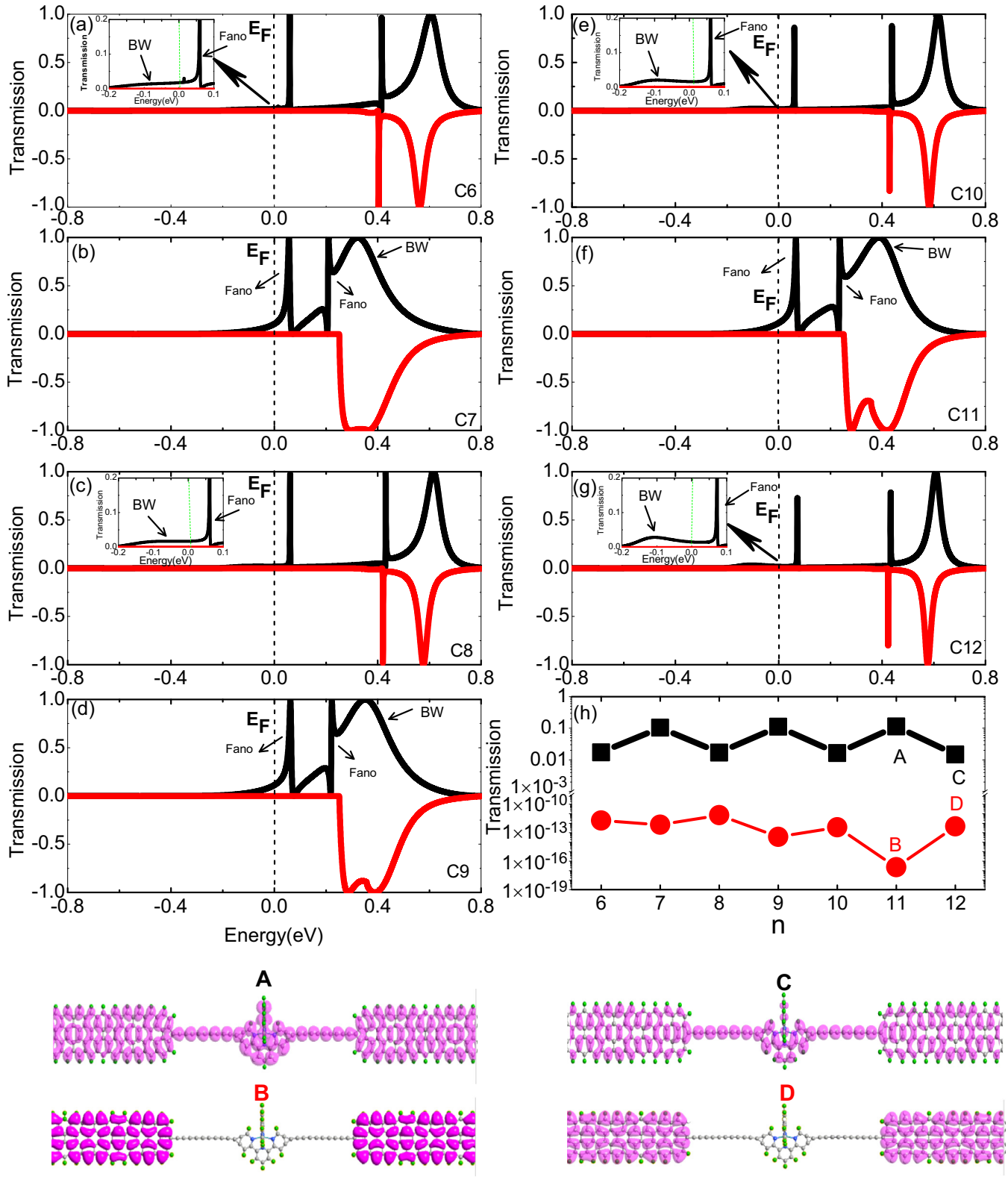

FIG. 2. (a)–(g) Spin-resolved transmission probabilities for the Ru-terpyridine molecular device. Here the number of the carbon atoms in the CACs N is taken from six to 12. The Fermi level is set to be zero (green dashed lines). The black and red lines denote the spin-up and spin-down channels, respectively. (h) Spin-resolved transmission probabilities at the Fermi level versus the length of the carbon atomic chain. The local density of states at points A–D are plotted in the bottom panel.

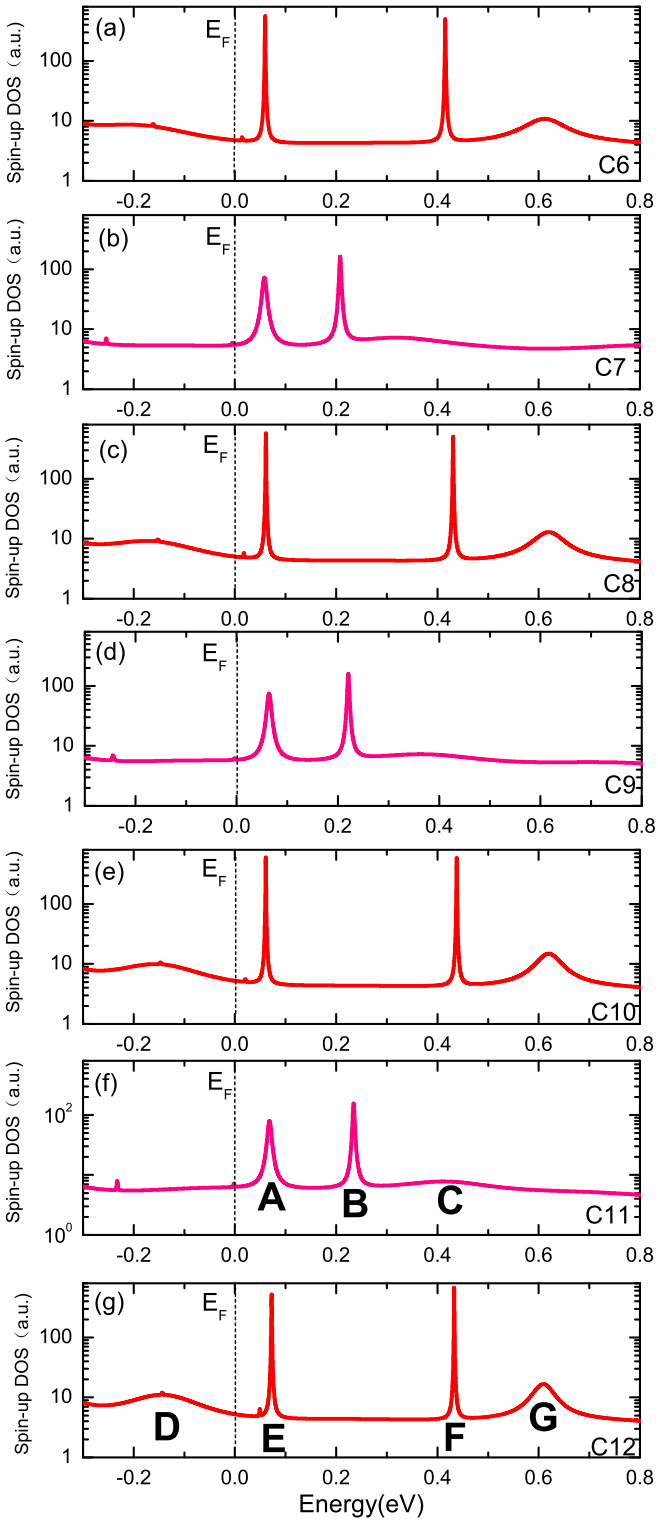

FIG. 3. The density of states (DOSs) of the Ru-terpyridine molecular devices versus the energy. From top to bottom, the number of the carbon atoms (N) is taken from six to 12.

To reveal the underlying reason of these Fano resonance peaks, we have given a log plot of the spin-up density of states (DOSs) as a function of the energy of Ru-terpyridine molecular devices containing CACs with different lengths in Fig. 3. It is found that some spin-up DOS peaks with different

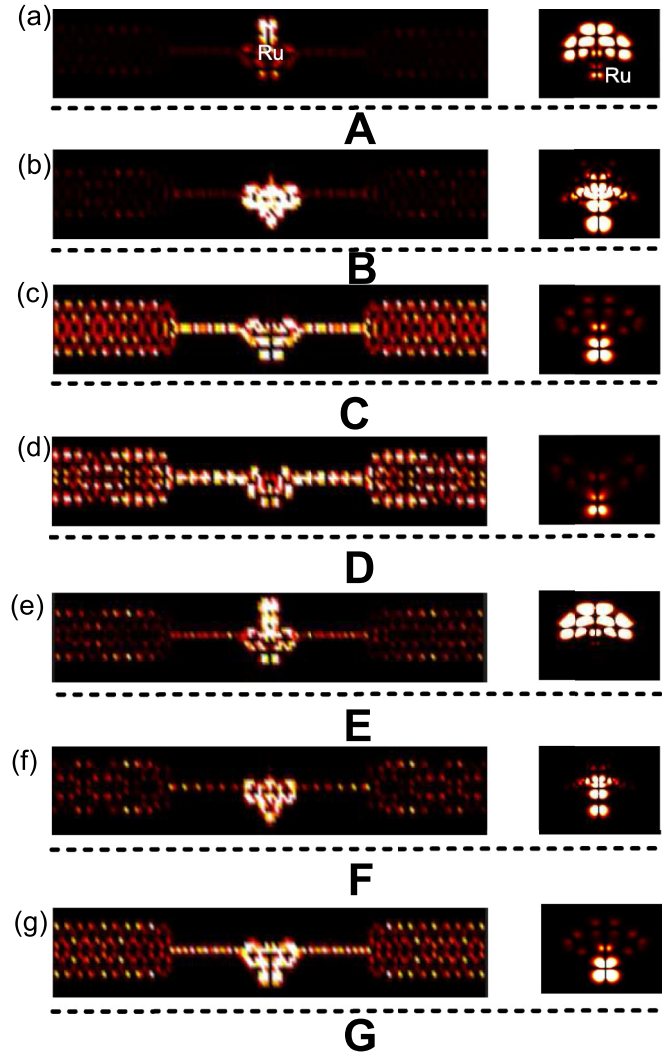

FIG. 4. The charge density of the molecular orbital states in the *yz* plane for energy points A–G.

broadenings are observed in the Ru-terpyridine molecular devices. The wider DOS peaks correspond to the strongly coupled electronic states and the narrower DOS peaks mean the weakly coupled electronic states. Quantum interference effects between the strongly coupled electronic states [e.g., C in Fig. 3(f) and D, G in Fig. 3(g)] and weakly coupled electronic states [e.g., A, B in Fig. 3(f) and E, F in Fig. 3(g)] results in the appearance of the Fano resonance in the vicinity of the narrower DOS peaks. The underlying physical mechanism is that the phase shift of π is generated when the energy sweeps across the weakly coupled electronic states, whereas a small variance appears in the phase for the strongly coupled electronic states. In addition, we also find that a strongly coupled electronic state appears below the Fermi level for the even-numbered CACs, while it is not observed in the odd-numbered CACs. Therefore, an odd-even oscillating behavior of the spin-up transmission probability is observed at the Fermi level. As an example, the charge density of the molecular orbital states at points A–G [labeled in Figs. 3(f) and 3(g)] are projected on the *yz* plane in Fig. 4. From these results, we can see that the strongly coupled electronic states

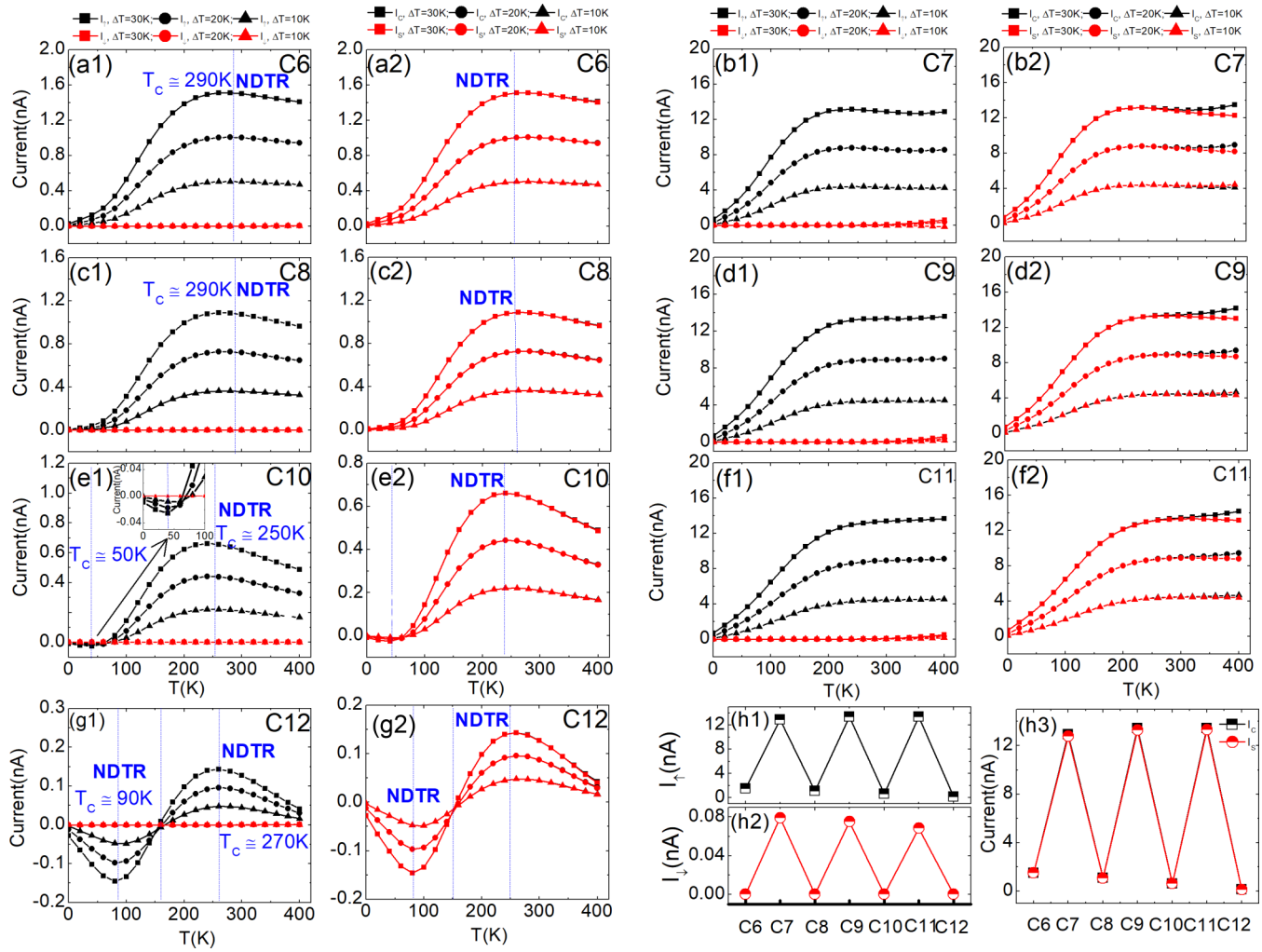

FIG. 5. (a1)–(g1) The spin-up current ($I_\uparrow$) and spin-down current ($I_\downarrow$) as functions of T at different ΔT. (a2)–(g2) The charge current (I_C) and spin current (I_S) as functions of T at different ΔT. (h1) The spin-up current $I_\uparrow$ and spin-down current $I_\downarrow$ as functions of the length of CACs at $T = 300$ K and $\Delta T = 30$ K. (h3) The corresponding charge current (I_C) and spin current (I_S) as functions of the length of CACs.

at C, D, and G spread over the whole scattering region, indicating that the effective couplings between the Ru-terpyridine molecule and CACs appear in the two-probe device. However, the localized states at A, B, E, and F are mainly located in the Ru-terpyridine molecule. For the localized states A and E, the spin-up charge density is mainly centered in the TRL_2 of the Ru-terpyridine molecule, and for the localized states B and F, the spin-up charge density is mainly centered in the TRL_1 of the Ru-terpyridine molecule.

When a temperature difference is applied across the Ru-terpyridine molecular devices, the current may be generated. In the absence of the electric bias, the transmission function near the Fermi level is of paramount importance to transport properties. Using Eq. (2), we can calculate the spin-resolved current induced by the temperature difference between the two ZGNR electrodes (here $T_L = T + \Delta T$ and $T_R = T$). Figures 5(a1)–5(g1) display the spin-up current $I_\uparrow$ and spin-down current $I_\downarrow$ of the Ru-terpyridine molecular devices containing the CACs with different lengths as a function of T, where ΔT is taken to be 10 K, 20 K, and 30 K, respectively. The corresponding charge current $I_C(=I_\uparrow + I_\downarrow)$ and spin current $I_S(=I_\uparrow - I_\downarrow)$ as a function of T are shown in Figs. 5(a2)–5(g2). It is found that the spin-down current in all Ru-terpyridine molecular devices is nearly suppressed to zero in the temperature range from 0 to 400 K, while the spin-up current always has a finite value, resulting in that I_C is nearly equal to I_S. Therefore, Ru-terpyridine molecular devices can be employed to design the spin caloritronic devices to generate the spin-polarized current with 100% spin polarization. Another key finding is that the NDTR in the spin-up current appears in the Ru-terpyridine molecular devices with the even-numbered CACs. As shown in Figs. 5(a1), 5(c1), 5(e1), and 5(g1), the spin-up current shows an obvious nonlinearity as T increases. For the $C4$ and $C6$ Ru-terpyridine molecular devices, we note that the spin-up current has a positive value, which is gradually enhanced with the increase of T and ΔT. When T is further increased [$T > T_c(=290$ K)], $I_\uparrow$ is slightly lowered. Thus the NDTR is achieved. For the $C8$ and $C10$ Ru-terpyridine molecular devices, $I_\uparrow$ has a negative value in the beginning. The magnitude of $I_\uparrow$ is first increased and then decreased as T increases. When $T > T_c(=50$ K) for $C8$ and $T > T_c(=90$ K) for $C10$, the NDTR is observed. After that,

the spin-up current becomes positive and the NDTR occurs again if T is larger than $T_c = 250$ K for $C8$ and $T_c = 270$ K for $C10$. Since $I_\downarrow$ is almost completely suppressed, the charge (spin) current has the same magnitude and trend with the spin-up current as T increases, as shown in Figs. 5(a2), 5(c2), 5(e2), and 5(g2). For the odd-numbered CACs, the spin-down current always keeps a very small value, while the spin-up current is first increased linearly and then arrives at a saturation value. Therefore, a perfect spin-filtering effect is achieved for all these Ru-terpyridine molecular devices. Here one should note that the NDTR is unlikely to appear in the odd-numbered CACs. The spin-up and spin-down currents as a function of the number of the carbon atoms in the CACs at $T = 300$ K and $\Delta T = 30$ K are plotted in Figs. 5(h1) and 5(h2), respectively. A similar odd-even oscillating behavior with Fig. 2(h) is observed, where a large spin-up current appears in the Ru-terpyridine molecular devices with the odd-numbered CACs, and a low spin-up current is obtained in the Ru-terpyridine molecular devices with the even-numbered CACs. Since the magnitude of the spin-up current is far larger than that of the spin-down current, $|I_C|$ is nearly equal to $|I_S|$, as shown in Fig. 5(h3).

To understand the NDTR and the sign change of the spin-up current in the C12 Ru-terpyridine molecular device, we choose four temperature points in the current curve, as shown in Fig. 6(a). A theoretical model for the two-probe device is proposed in Fig. 6(b), where the left and right electrodes are represented by the their Fermi distribution functions and the central scattering region is modeled by the transmission function (as an example, we choose $\tau_\uparrow$ for the C12 Ru-terpyridine molecular device). When there exists a temperature difference between the left and right ZGNR electrodes, a nonequilibrium system is formed. Here the difference of electron densities between the left and right electrodes is determined by the Fermi distribution difference $\Delta f[=f_L(\epsilon, T + \Delta T) - f_R(\epsilon, T)]$. Above the Fermi level, Δf is positive for $\Delta T > 0$, meaning that carriers (electrons) may flow from the left electrode to the right electrode through the Ru-terpyridine molecule. As a result, the electron current $I_\uparrow^+$ is achieved [see Fig. 6(b)]. However, below the Fermi level, Δf is negative for $\Delta T > 0$, meaning that the carriers (holes) may flow from the right electrode to the left electrode through the Ru-terpyridine molecule. As a result, the hole current $I_\uparrow^-$ is achieved [see Fig. 6(b)]. The total current $I_\uparrow$ is determined by the sum of the electron current $I_\uparrow^+$ and the hole current $I_\downarrow^-$. One should note that $I_\uparrow^+$ and $I_\uparrow^-$ may cancel out if the spin-up transmission function is energy independent. However, as shown in the middle of Fig. 6(b), the spin-up transmission function near the Fermi level is composed of the BW resonance peak below the Fermi level and the Fano resonance peak above the Fermi level. Such a feature indicates that the BW resonance peak is responsible for the hole current $I_\uparrow^-$, while the Fano resonance peak plays a critical part in the electron current $I_\uparrow^+$. If $I_\uparrow^+$ has a larger contribution than $I_\uparrow^-$ for the total current, the net spin-up current is positive. Conversely, the spin-up current will become negative when $I_\uparrow^-$ has main contributions. To further illustrate this point, we plot the spectral current $J_\uparrow[=\tau_\uparrow(f_L(\epsilon, T + \Delta T) - f_R(\epsilon, T))]$ versus the energy at different T with $\Delta T = 30$ K in Fig. 6(c). It should be noted that these interesting thermal spin-transport properties in molecular devices can be well understood from the numerical integrations of the spin-dependent spectral currents in the whole energy region. Due to the exponential decaying nature of the Fermi-Dirac distribution function, only the transmission function near the Fermi level has a large contribution to the net current. When $T_A = 80$ K, the BW resonance peak has the main contribution to the spin-up current, resulting in a large negative peak below the Fermi level and a relatively small positive peak in the spectral current above Fermi level. Therefore, the Fano resonance peak has almost no contribution to $I_\uparrow$. In this case, the contribution of $I_\uparrow^-$ to $I_\uparrow$ is larger than of $I_\uparrow^+$ to $I_\uparrow$, leading to a negative hole current. As T increases, the Fermi dirac distribution is broadened, which will overlap the Fano resonance peak. Thus, we also note that the peak of $J_\uparrow$ induced by the Fano resonance is obviously enhanced as T increases. Therefore, $I_\uparrow$ is firstly suppressed. At $T_B = 157$ K, the magnitude of $I_\uparrow^+$ is nearly equal to that of $I_\uparrow^-$, resulting in a zero net spin-up current. As T is further increased, $I_\uparrow^+$ dominates the

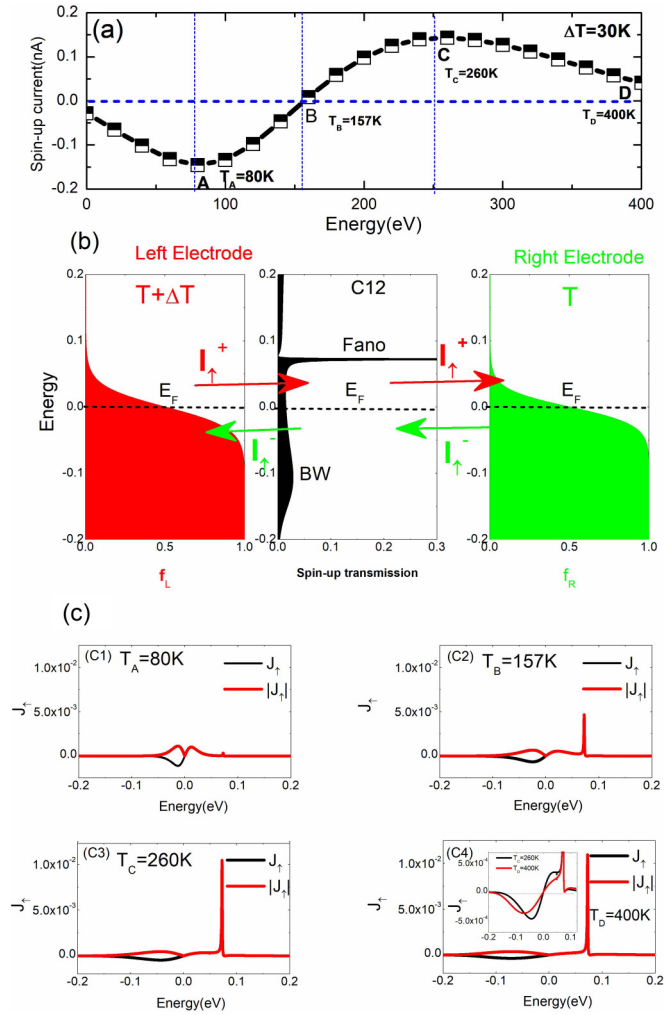

FIG. 6. (a) The spin-up current ($I_\uparrow$) as a function of T at $\Delta T = 30$ K in the C12 Ru-terpyridine molecular devices. (b) A theoretical model that used to explain the mechanism of the NDTR. (c) The corresponding spin-up spectral current ($J_\uparrow$) as a function of the energy at $T = 80$ K, 157 K, 260 K, and 400 K, respectively.

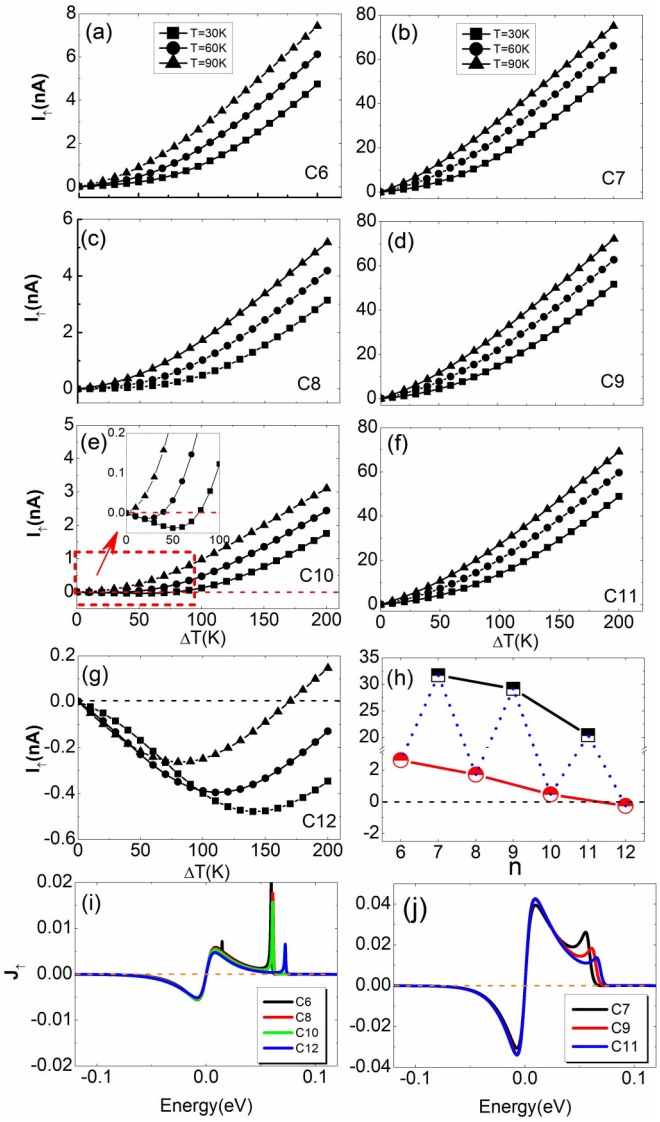

FIG. 7. (a)–(g) The spin-up current ($I_\uparrow$) as a function of ΔT at different T in the C6–C12 Ru-terpyridine molecular devices, respectively. (h) At $\Delta T = 150$ K and $T = 30$ K, the spin-up current ($I_\uparrow$) versus the length of the CACs. (i), (j) The spin-up spectral current ($J_\uparrow$) versus the energy at $\Delta T = 150$ K and $T = 30$ K for the even-numbered and odd-numbered CACs, respectively.

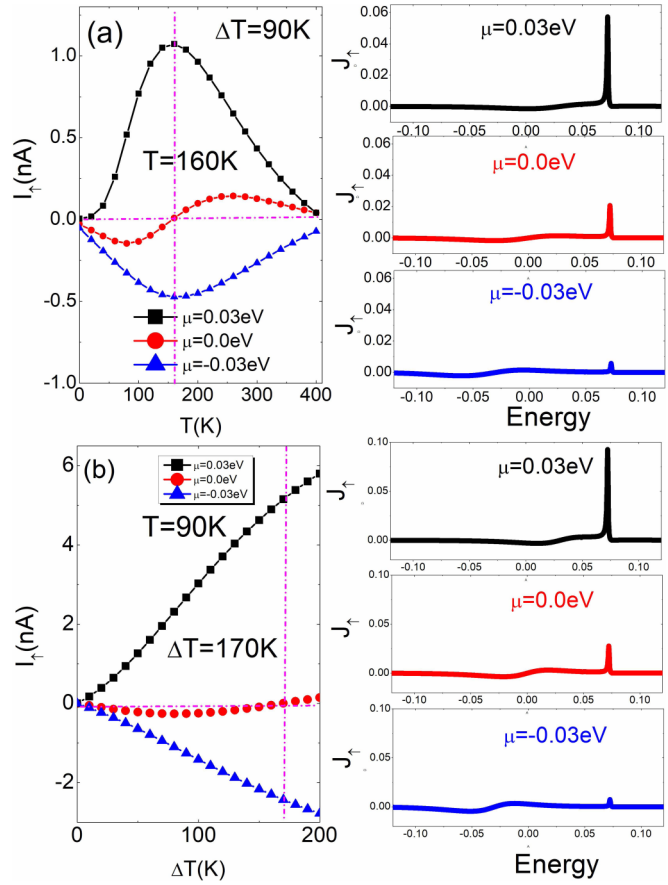

FIG. 8. Left panel: (a) The spin-up current ($I_\uparrow$) as a function of T at $\Delta T = 90$ K in the C12 Ru-terpyridine molecular device. (b) The spin-up current ($I_\uparrow$) as a function of ΔT at $T = 90$ K in the C12 Ru-terpyridine molecular device. Right panel: The corresponding spin-up spectral current ($J_\uparrow$) versus the energy at $T = 160$ K and $\Delta T = 90$ K (upper panel) and $T = 90$ K and $\Delta T = 170$ K (bottom panel).

contribution for $I_\uparrow$, and in this case $I_\uparrow$ becomes positive, and a net electron current is achieved. When $T = 260$ K, $I_\uparrow$ reaches a peak value, then it is suppressed as T is furthered increased. A NDTR is observed. To give a reasonable explanation, we plot $J_\uparrow$ versus energy for $T_C = 260$ K and $T_D = 400$ K in the inset of Fig. 6(c4). By comparing the data, we note that $J_\uparrow$ from the BW resonance peak above the Fermi level is obviously suppressed. This fact results in the decrease for the net spin-up current at $T_D = 400$ K.

Figures 7(a)–7(g) show the net spin-up current $I_\uparrow$ of the Ru-terpyridine molecular device containing the CACs with different lengths versus the temperature difference ΔT at different T. Obviously, in C10 and C12 Ru-terpyridine molecular devices, $I_\uparrow$ has a negative value in the beginning, and then it reaches a peak value. After that, it is suppressed as ΔT is further increased. Therefore, a NDTR appears in even-numbered CACs with long lengths. For other Ru-terpyridine molecular devices, $I_\uparrow$ shows a monotonically increasing trend as ΔT increases. When ΔT is fixed, $I_\uparrow$ is also enhanced as T increases. At $\Delta T = 150$ K and $T = 30$ K, $I_\uparrow$ shows an odd-even oscillating behavior as the length of CACs increases, in which a large current appears in the odd-numbered CACs and a small current appears in the even-numbered CACs. In addition, we also note that $I_\downarrow$ is slightly suppressed. To explain the above transport properties, we plot the spectral current of these Ru-terpyridine molecular devices at $\Delta T = 150$ K and $T = 30$ K. For the even-numbered CACs, $J_\uparrow$ above the Fermi level has a stronger suppression than that below the Fermi level as the length increases [see Fig. 7(i)]. Similar results are also observed in the odd-numbered CACs, as shown in Fig. 7(j). Thus, the spin-up current becomes smaller and smaller as the length increases [see Fig. 7(h)]. Especially, for the C12 Ru-terpyridine molecular device, the peak of $J_\uparrow$ induced by the Fano resonance is obviously suppressed, resulting in a negative net spin-up current, In this case, $I_\uparrow^-$ has a larger contribution to $I_\uparrow$ than $I_\uparrow^+$.

Finally, we explore the effect of the Fermi level to the net spin-up current in the C12 Ru-terpyridine molecular device.

In Fig. 8(a), the spin-up current as a function of T with $\Delta T = 90$ K under different Fermi levels is plotted, and the results show that the sign and magnitude of $I_\uparrow$ can be effectively tuned. The obvious NDTR is also observed. To further understand these transport properties, the spectral current $J_\uparrow$ versus the energy at different Fermi levels is shown in the right panel of Fig. 8(a), and here T is fixed at 160 K. Obviously, the peak of $J_\uparrow$ induced by the Fano resonance is enhanced when the Fermi level is close to the Fano resonance, thus $I_\uparrow^+$ plays a key role in the spin-up current, resulting in a positive current. Figure 8(b) shows the spin-up current as a function of ΔT with $T = 90$ K. Similar results are found, and NDTR only appears when $\mu = 0$. The spectral current $J_\uparrow$ with $T = 160$ K is plotted in the right panel of Fig. 8(b), which can explain the above results well. Here $I_\uparrow^+$ dominates $I_\uparrow$ when the Fermi level is close to Fano resonance ($\mu = 0.3V$), and $I_\uparrow^-$ dominates $I_\uparrow$ when the Fermi level is close to BW resonance ($\mu = -0.3V$).

IV. CONCLUSIONS

We have investigated thermally driven spin-transport properties of Ru-terpyridine molecular devices containing CACs with different lengths. An odd-even oscillating behavior in the spin-resolved transmission spectra at the Fermi level and the NDTR easily appear in long even-numbered CACs. Moreover, the sign of the thermally driven current can be changed by the temperature. We attribute the behavior to the competition between the BW and Fano resonances in the vicinity of the Fermi level for the contributions of the thermally driven current.

ACKNOWLEDGMENTS

The authors thank the support of the National Natural Science Foundation of China (NSFC) (Grant No. 61674022), the Natural Science Foundation of Jiangsu Province (Grant No. BK20171243), and the Key Project of Natural Science Research in Colleges and Universities (Grant No. 17KJA480001). X.F.Y. thanks the support of the Qing Lan Project of Jiangsu Province. Y.S.L. also thanks the support of the Qing Lan Project of Jiangsu Province. This paper is also supported by the outstanding scientific and technological innovation team of Jiangsu Province.

[1] A. Aviram and M. A. Ratner, Molecular rectifiers, Chem. Phys. Lett. **29**, 277 (1974).
[2] J. Chen, M. A. Reed, A. M. Rawlett, and J. M. Tour, Large on-off ratios and negative differential resistance in a molecular electronic device, Nature **455**, 778 (2008).
[3] Y. C. Chen and M. Di Ventra, Effect of Electron-Phonon Scatteringand Shot Noise in Nanoscale Junctions, Phys. Rev. Lett. **95**, 166802 (2005).
[4] Y. S. Kim, A. Lenert, E. Meyhofer, and P. Reddy, Temperature dependence of thermopower in molecular junctions, Appl. Phys. Lett. **109**, 033102 (2016).
[5] R. J. Miao, H. L. Xu, M. Skripni, L. J. Cui, K. Wang, K. G. L. Pedersen, M. Leijnse, F. Pauly, Kenneth Wärnma, E. Meyhofer, P. Reddy, and H. Linke, Influence of quantum interference on the thermoelectric properties of molecular junctions, Nano Lett. **18**, 5666 (2018).
[6] K. Wang, E. Meyhofer, and P. Reddy, Thermal and thermoelectric properties of molecular junctions, Adv. Funct. Mater. **30**, 1904534 (2019).
[7] Y. S. Liu and Y. C. Chen, Single-molecule refrigerators: Substitution and gate effects, Appl. Phys. Lett. **98**, 213103 (2011).
[8] U. Fano, Effects of configuration interactions on intensities and phase shifts, Phys. Rev. **124**, 1866 (1961).
[9] R. P. Madden and K. Codling, New Autoionizing Atomic Energy Levels in He, Ne, and Ar, Phys. Rev. Lett. **10**, 516 (1963).
[10] S. Fan, W. Suh, and J. Joannopoulos, Temporal coupled-mode theory for the Fano resonance in optical resonators, J. Opt. Soc. Am. **20**, 569 (2003).
[11] K. Kobayashi, H. Aikawa, S. Katsumoto, and Y. Iye, Tuning of the Fano Effect Through a Quantum Dot in an Aharonov-Bohm Interferometer, Phys. Rev. Lett. **88**, 256806 (2002).
[12] H. Z. Lu, R. Lü, and B. F. Zhu, Tunable Fano effect in parallel-coupled double quantum dot system, Phys. Rev. B **71**, 235320 (2005).
[13] Y. Q. Li, G. S. Feng, J. Z. Wu, J. Ma, B. Deb, A. Pal, L. T. Xiao, and S. T. Jia, Fano effect in an ultracold atom-molecule coupled system, Phys. Rev. A **99**, 022702 (2019).
[14] C. F. Fang, D. M. Li, B. Cui, Y. Q. Xu, G. M. Ji, and D. S Liu, Effect of different electrodes on Fano resonance in molecular devices, Appl. Phys. Lett. **100**, 023303 (2012).
[15] C. M. Finch, V. M. García-Suárez, and C. J. Lambert, Giant thermopower and figure of merit in single-molecule devices, Phys. Rev. B **79**, 033405 (2009).
[16] Y. S. Liu and X. F. Yang, Enhancement of thermoelectric efficiency in a double-quantum-dot molecular junction, J. Appl. Phys. **108**, 023710 (2010).
[17] Y. S. Liu, F. Chi, X. F. Yang, and J. F. Feng, Pure spin thermoelectric generator based on a Rashba quantum dot molecule, J. Appl. Phys. **109**, 053712 (2011).
[18] F. Prins, A. Barreiro, J. W. Ruitenberg, J. S. Seldenthuis, N. Aliaga-Alcalde, L. M. K. Vandersypen, and H. S. J. van der Zant, Room-temperature gating of molecular junctions using few-layer graphene nanogap electrodes, Nano Lett. **11**, 4607 (2011).
[19] C. C. Jia, A. Migliore, N. Xin, S. Y. Huang, J. Y. Wang, Q. Yang, S. P. Wang, H. L. Chen, D. M. Wang, B. Y. Feng, Z. R. Liu, G. Y. Zhang, D. H. Qu, H. Tian, Mark A. Ratner, H. Q. Xu, A. Nitzan, and X. F. Guo, Covalently bonded single-molecule junctions with stable and reversible photoswitched conductivity, Science **352**, 1443 (2016).
[20] L. N. Meng, N. Xin, C. Hu, J. Y. Wang, B. Gui, J. J. Shi, C. Wang, C. Shen, G. Y. Zhang, H. Guo, S. Meng, and X. F. Guo, Side-group chemical gating via reversible optical and electric control in a single molecule transistor, Nat. Commun. **10**, 1450 (2019).
[21] H. Q. Wan, B. H. Zhou, X. W. Chen, C. Q. Chen, and G. H. Zhou, Switching, dual spin-filtering effects, and negative differential resistance in a carbon-based molecular device, J. Phys. Chem. C **116**, 2570 (2012).

[22] Y. Cao, S. H. Dong, S. Liu, Z. F. Liu, and X. F. Guo, Toward functional molecular devices based on graphene-molecule junctions, Angew. Chem. **125**, 3998 (2013).

[23] P. Song, S. Guerin, S. J. R. Tan, H. V. Annadata, X. J. Yu, M. Scully, Y. M. Han, M. Roemer, K. Ping Loh, D. Thompson, and Christian A. Nijhuis, Stable molecular diodes based on π-π interactions of the molecular frontier orbitals with graphene electrodes, Adv. Mater. **30**, 1706322 (2018).

[24] Y. W. Son, M. L. Cohen, and S. G. Louie, Energy Gaps in Graphene Nanoribbons, Phys. Rev. Lett. **97**, 216803 (2006).

[25] A. Saraiva-Souza, M. Smeu, L. Zhang, A. G. Souza Filho, H. Guo, and M. A. Ratner, Molecular spintronics: Destructive quantum interference controlled by a gate, J. Am. Chem. Soc. **136**, 15065 (2014).

[26] X. F. Yang, H. L. Wang, Y. S. Chen, Y. W. Kuang, X. K. Hong, Y. S. Liu, J. F. Feng, and X. F. Wang, Perfect spin filtering and large spin thermoelectric effects in organic transition-metal molecular junctions, Phys. Chem. Chem. Phys. **17**, 22815 (2015).

[27] K. Uchida, S. Takahashi, K. Harii, J. Ieda, W. Koshibae, K. Ando, S. Maekawa, and E. Saitoh, Observation of the spin Seebeck effect, Nature **455**, 778 (2008).

[28] K. Uchida, J. Xiao, H. Adachi, J. Ohe, S. Takahashi, J. Ieda, T. Ota, Y. Kajiwara, H. Umezawa, H. Kawai, G. E. W. Bauer, S. Maekawa, and E. Saitoh, Spin Seebeck insulator, Nat. Mater. **9**, 894 (2010).

[29] C. M. Jaworski, J. Yang, S. Mack, D. D. Awschalom, J. P. Heremans, and R. C. Myers, Observation of the spin-Seebeck effect in a ferromagnetic semiconductor, Nat. Mater. **9**, 898 (2010).

[30] S. M. Wu, W. Zhang, K. C. Amit, P. Borisov, J. E. Pearson, J. Samuel Jiang, D. Lederman, A. Hoffmann, and A. Bhattacharya, Antiferromagnetic Spin Seebeck Effect, Phys. Rev. Lett. **116**, 097204 (2016).

[31] T. Kikkawa, K. Uchida, Y. Shiomi, Z. Qiu, D. Hou, D. Tian, H. Nakayama, X. F. Jin, and E. Saitoh, Longitudinal Spin Seebeck Effect Free from the Proximity Nernst Effect, Phys. Rev. Lett. **110**, 067207 (2013).

[32] Y. S. Liu, X. F. Yang, F. Chi, M. S. Si, and Y. Guo, A proposal for time-dependent pure-spin-current generators, Appl. Phys. Lett. **101**, 213109 (2012).

[33] D. Wu, X. H. Cao, S. Z. Chen, L. M. Tang, Y. X. Feng, K. Q. Chen, and W. Zhou, Pure spin current generated in thermally driven molecular magnetic junctions: A promising mechanism for thermoelectric conversion, J. Mater. Chem. A **7**, 19037 (2019).

[34] C. Jin, H. Lan, L. Peng, K. Suenaga, and S. Iijima, Deriving Carbon Atomic Chains from Graphene, Phys. Rev. Lett. **102**, 205501 (2009).

[35] A. Chuvilin, J. C. Meyer, G. Algara-Siller, and U. Kaiser, From graphene constrictions to single carbon chains, New J. Phys. **11**, 083019 (2009).

[36] O. Cretu, A. R. Botello-Mendez, I. Janowska, C. Pham-Huu, J. Charlier, and F. Banhart, Electrical transport measured in atomic carbon chains, Nano Lett. **13**, 3487 (2013).

[37] J. Taylor, H. Guo, and J. Wang, *Ab initio* modeling of quantum transport properties of molecular electronic devices, Phys. Rev. B **63**, 245407 (2001).

[38] M. Brandbyge, J. L. Mozos, P. Ordejón, J. Taylor, and K. Stokbro, Density-functional method for nonequilibrium electron transport, Phys. Rev. B **65**, 165401 (2002).

[39] S. Datta, *Electronic Transport in Mesoscopic Systems*, Cambridge Studies in Semiconductor Physics and Microelectronic Engineering (Cambridge University Press, New York, 1997).

[40] Y. S. Liu, X. F. Wang, and F. Chi, Non-magnetic doping induced a high spin-filter efficiency and large spin Seebeck effect in zigzag graphene nanoribbons, J. Mater. Chem. C **1**, 8046 (2013).

[41] K. Wakabayashi, M. Fujita, H. Ajiki, and M. Sigrist, Electronic and magnetic properties of nanographite ribbons, Phys. Rev. B **59**, 8271 (1999).

[42] Z. Y. Li, H. Y. Qian, J. Wu, B. L. Gu, and W. H. Duan, Role of Symmetry in the Transport Properties of Graphene Nanoribbons Under Bias, Phys. Rev. Lett. **100**, 206802 (2008).